CrossMark

FRB 190520B Embedded in a Magnetar Wind Nebula and Supernova Remnant: A Luminous Persistent Radio Source, Decreasing Dispersion Measure, and Large Rotation Measure

Z. Y. Zhao[1] and F. Y. Wang[1,2]
[1] School of Astronomy and Space Science, Nanjing University, Nanjing 210093, People's Republic of China; fayinwang@nju.edu.cn
[2] Key Laboratory of Modern Astronomy and Astrophysics (Nanjing University), Ministry of Education, Nanjing 210093, People's Republic of China

Abstract

Recently, FRB 190520B, which has the largest extragalactic dispersion measure (DM), was discovered by the Five-hundred-meter Aperture Spherical radio Telescope (FAST). The DM excess over the intergalactic medium and Galactic contributions is estimated as $\sim 900 \, \mathrm{pc \, cm^{-3}}$, which is nearly ten times higher than that of other fast-radio-burst (FRB) host galaxies. The DM decreases with the rate $\sim 0.1 \, \mathrm{pc \, cm^{-3}}$ per day. It is the second FRB associated with a compact persistent radio source (PRS). The rotation measure (RM) is found to be larger than $1.8 \times 10^5 \, \mathrm{rad \, m^{-2}}$. In this Letter, we argue that FRB 190520B is powered by a young magentar formed by core collapse of massive stars, embedded in a composite of a magnetar wind nebula (MWN) and supernova remnant (SNR). The energy injection of the magnetar drives the MWN and SN ejecta to evolve together and the PRS is generated by the synchrotron radiation of the MWN. The magnetar has an interior magnetic field $B_{\mathrm{int}} \sim (2\text{--}4) \times 10^{16} \, \mathrm{G}$ and an age $t_{\mathrm{age}} \sim 14\text{--}22 \, \mathrm{yr}$. The dense SN ejecta and the shocked shell contribute a large fraction of the observed DM and RM. Our model can naturally and simultaneously explain the luminous PRS, decreasing DM, and extreme RM of FRB 190520B.

Unified Astronomy Thesaurus concepts: Radio bursts (1339); Radio transient sources (2008); Magnetars (992); Supernova remnants (1667)

1. Introduction

Fast radio bursts (FRBs) are mysterious radio transients with millisecond duration (Lorimer et al. 2007) whose physical origins are still unknown, though they were first reported more than a decade ago (Katz 2018; Cordes & Chatterjee 2019; Zhang 2020; Petroff et al. 2021; Xiao et al. 2021). Their large dispersion measures (DMs) well above the contribution from the Milky Way imply they may originate at cosmological distances. Some FRBs show repeating bursts and others seem to be one-off events. Many models have been proposed to interpret the origins of FRBs (see Platts et al. 2019 for a recent review). Among those models, the ones relating to magnetars are promising because of the detection of FRB 200428 from a Galactic magnetar (Bochenek et al. 2020; CHIME/FRB Collaboration et al. 2020a).

Recently, the repeating FRB 190520B, which has the largest extragalactic DM thus far was discovered by the Five-hundred-meter Aperture Spherical radio Telescope (FAST) (Niu et al. 2021). It is located in a dwarf galaxy with a high star formation rate and it is associated with a compact, luminous ($\nu L_\nu \sim 10^{39} \, \mathrm{erg \, s^{-1}}$), persistent radio source (PRS), which is too luminous to come from the star formation activity of the host galaxy (Law et al. 2021). From the observations of the Karl G. Jansky Very Large Array (VLA), the power-law spectral index of the compact PRS has been found to be -0.41 ± 0.04. This is the second PRS associated with FRBs; the other is FRB 121102 (Chatterjee et al. 2017). The similarity between the two PRSs indicates that they have similar physical

origins. Interestingly, a similar PRS is associated with the type I superluminous supernova (SLSN) PTF10hgi, but it is less luminous ($\nu L_\nu \sim 10^{38} \, \mathrm{erg \, s^{-1}}$) than those of FRBs (Eftekhari et al. 2019). From a comparative study between the wide-band spectrum of PTF10hgi and FRB 121102, Mondal et al. (2020) found that the PRS most probably originates from a pulsar/magnetar wind nebula (PWN/MWN). In this work, we focus on PRSs associated with FRBs.

When a pulsar-driven relativistic wind interacts with the surrounding medium, it generates a luminous PWN. For rapidly rotating pulsars, the rotational energy is the main reservoir for powering the wind nebula, which has been well studied for Galactic PWNe (Tanaka & Takahara 2010). Some FRBs' energy injection (Li et al. 2020) and rotational-energy-injection (Kashiyama & Murase 2017; Dai et al. 2017; Yang & Dai 2019; Wang & Lai 2020) models have been proposed. However, for a decades-old magnetar, the rotational energy is less significant than the interior magnetic energy. A case of magnetic-energy injection was proposed which successfully explains the PRS's luminosity and the large rotation measure (RM, Michilli et al. 2018; Hilmarsson et al. 2021) of FRB 121102 (Margalit & Metzger 2018).

From the estimation of Niu et al. (2021), the DM of the host galaxy is $\mathrm{DM_{host}} \sim 900 \, \mathrm{pc \, cm^{-3}}$, which is nearly ten times higher than other FRBs' host galaxies. However, using the state-of-the-art IllustrisTNG simulation, Zhang et al. (2020) showed that the DM contributed by FRB 190520B-like host galaxies at $z \sim 0.2$ is $\sim 50\text{--}250 \, \mathrm{pc \, cm^{-3}}$. Unlike the the increasing DM of FRB 121102 (Hessels et al. 2019; Josephy et al. 2019; Oostrum et al. 2020; Li et al. 2021) and the nearly unchangeable DM of FRB 180916 (CHIME/FRB Collaboration et al. 2020b; Pastor-Marazuela et al. 2021; Nimmo et al. 2021), the DM of FRB 190520B decreases at a rate of

$-0.09 \pm 0.02 \, \mathrm{pc \, cm^{-3} \, day^{-1}}$ (Niu et al. 2021). Under the assumption of 100% intrinsic, linear polarization, the low limit of RM is $> 1.8 \times 10^5 \, \mathrm{rad \, m^{-2}}$ (Niu et al. 2021), which is larger than that of FRB 121102. The large DM and RM, together with the decreasing DM, may come from the expanding shocked shell of a supernova remnant (SNR, see Yang & Zhang 2017; Piro & Gaensler 2018; Katz 2021a; Zhao et al. 2021). Katz (2021a) rejected the possibility that the large host DM of FRB 190520B is contributed by interstellar clouds and proposed that the excess of the host DM can be attributed to a young SNR.

In this Letter, we propose that the magnetar associated with FRB 190520B is embedded in a composite of an MWN and an SNR. The magnetar is formed by the core collapse of a massive star. Due to the energy injection of the young magnetar, the wind nebula and the SN ejecta evolve together. The observed PRS is produced by the synchrotron radiation of the nebula. Our numerical calculations are based on the spectral evolution model of Galactic PWNe (Tanaka & Takahara 2010, 2013) with magnetic-energy injection (Margalit & Metzger 2018). The dense SNR ejecta and the shocked shell contribute considerable DM and RM. With the expansion of the SNR, the DM will decrease rapidly, similar to the observed trend. Our model can simultaneously explain the luminous PRS, decreasing DM, and extreme RM of FRB 190520B.

This Letter is organized as follows. In Section 2, the synchrotron spectral evolution model from MWN is shown. We present our numerical results of the PRS energy spectrum in Section 3. The long-term DM evolution model explaining FRB 190520B is shown in Section 4. Finally, we give a summary in Section 5.

2. The Compact Persistent Radio Source

The compact PRS associated with FRBs is from synchrotron radiation from the MWN powered by the young magnetar in our model. Rotational or magnetic energy, together with the particle, is injected into the nebula, and the electron will undergo radiation or adiabatic cooling. In this section, we will introduce the cases of rotational and magnetic-energy injection, and give the explanation of the radio spectra of PRSs associated with FRB 190520B and FRB 121102.

2.1. Energy Injection

The case of rotational-energy injection is well studied for the wide-band spectrum of the Crab Nebula (Tanaka & Takahara 2010). The spin-down luminosity can be estimated as (Dai & Lu 1998; Zhang & Mészáros 2001; Murase et al. 2015)

$$
\begin{aligned}
L_{\mathrm{sd}} &= L_{\mathrm{sd},i}\left(1 + \frac{t}{t_{\mathrm{em}}}\right)^{-2} \\
&\simeq \begin{cases} 8.6 \times 10^{45} \mathrm{erg s^{-1}} P_{i,-2.5}^{-4} B_{\mathrm{dip},14}^2 & (t \leqslant t_{\mathrm{em}}) \\ 8.9 \times 10^{42} \mathrm{erg s^{-1}} B_{\mathrm{dip},14}^{-2} t_7^{-2} & (t > t_{\mathrm{em}}) \end{cases},
\end{aligned} \quad (1)
$$

where $t_{\mathrm{em}} \simeq 3.2 \times 10^5 B_{\mathrm{dip},14}^{-2} P_{i,-2.5}^2$ s is the characteristic spin-down timescale, B_{dip} is the magnetic dipole, and P_i is the initial spin period. The model of magnetic-energy injection has been proposed to explain the exceptionally high RM and PRS associated with FRB 121102 (Margalit & Metzger 2018). The interior magnetic energy (Katz 1982)

$$
\mathcal{E}_{\mathrm{B,int}} \simeq B_{\mathrm{int}}^2 R_{\mathrm{ns}}^3 / 6 \approx 3 \times 10^{49} B_{\mathrm{int},16}^2 \, \mathrm{erg}, \quad (2)
$$

is another ideal reservoir for PRS, where B_{int} is the interior magnetic field and $R_{\mathrm{ns}} = 12$ km is the neutron star radius. The magnetic-energy-injection luminosity can be written as (Margalit & Metzger 2018)

$$
L_{\mathrm{m}} = (\alpha - 1)\frac{\mathcal{E}_{\mathrm{B,int}}}{t_0}\left(\frac{t}{t_0}\right)^{-\alpha}, \quad (3)
$$

where t_0 is the onset of energy injection and $\alpha > 1$ is the power-law index.

The injected electron–positron pairs will be accelerated to relativistic energy by the termination shock before entering the nebula. Similar to Galactic PWNe (Tanaka & Takahara 2010, 2013), the injection particle spectrum is described as a broken power-law form

$$
Q_{\mathrm{inj}}(\gamma, t) = \begin{cases} Q_0(t)(\gamma/\gamma_{\mathrm{b}})^{-p_1} & \gamma_{\mathrm{min}} \leqslant \gamma \leqslant \gamma_{\mathrm{b}} \\ Q_0(t)(\gamma/\gamma_{\mathrm{b}})^{-p_2} & \gamma_{\mathrm{b}} \leqslant \gamma \leqslant \gamma_{\mathrm{max}} \end{cases}, \quad (4)
$$

where $Q_0(t)$ is the normalization factor and γ_{min}, γ_b, and γ_{max} are the minimum, break, and maximum Lorentz factors. p_1 and p_2 are the injection spectrum indices for low- and high-energy particles, respectively. The normalization factor is determined by

$$
\int_{\gamma_{\mathrm{min}}}^{\gamma_{\mathrm{max}}} Q_{\mathrm{inj}}(\gamma, t)\gamma m_e c^2 d\gamma = \epsilon_{\mathrm{e}} L(t), \quad (5)
$$

where ϵ_{e} is the electron energy fraction and $L(t)$ is the spin-down or magnetic-energy-injection luminosity.

2.2. Dynamics and the Nebular Magnetic Field Evolution

The inner density profile of the ejecta can be described as a smooth or flat power law (Chevalier & Soker 1989; Kasen & Bildsten 2010)

$$
\rho_{\mathrm{ej}} = \frac{(3 - \delta)M_{\mathrm{ej}}}{4\pi R_{\mathrm{ej}}^3}\left(\frac{R}{R_{\mathrm{ej}}}\right)^{-\delta}, \quad (6)
$$

where $\delta = 0$–1 is widely used, and we take $\delta = 1$ in this work. The ejecta will expand freely until the Sedov–Taylor phase without the energy injection. The initial velocity is $v_{\mathrm{ej},i} \sim 10{,}000 \, \mathrm{km \, s^{-1}} (\mathcal{E}_{\mathrm{SN}}/10^{51}\mathrm{erg})^{1/2}(M_{\mathrm{ej}}/M_\odot)^{-1/2}$ cm s^{-1}. When a newborn millisecond magnetar exists, the nebula and ejecta radius will evolve together because the injected energy will significantly accelerate the ejecta via magnetized wind. For $R_{\mathrm{n}} < R_{\mathrm{ej}}$, the nebula radius R_{n} is given by Metzger et al. (2014),

$$
\frac{dR_n}{dt} = \sqrt{\frac{7}{6(3 - \delta)}\frac{\mathcal{E}_{\mathrm{tot}}}{M_{\mathrm{ej}}}\left(\frac{R_n}{R_{\mathrm{ej}}}\right)^{3-\delta}} + \frac{R_n}{t}, \quad (7)
$$

where $\mathcal{E}_{\mathrm{tot}}$ is the total injection energy. If $R_{\mathrm{n}} > R_{\mathrm{ej}}$, the nebula and ejecta will move together

$$
\frac{\mathrm{d}R_{\mathrm{ej}}}{\mathrm{d}t} = \frac{\mathrm{d}R_{\mathrm{n}}}{\mathrm{d}t} = v_{\mathrm{ej},\mathrm{f}}, \quad (8)
$$

where $v_{\mathrm{ej},\mathrm{f}} = \sqrt{2(\mathcal{E}_{\mathrm{tot}} + \mathcal{E}_{\mathrm{SN}})/M_{\mathrm{ej}}}$ is the final accelerated velocity. For $t < t_0$, the rotational-energy injection dominates, and the injection energy is $\mathcal{E}_{\mathrm{tot}} = \mathcal{E}_{\mathrm{rot}} = \int_0^t L_{\mathrm{sd}}(t)\mathrm{d}t$. For $t > t_0$, the interior magnetic energy starts to leak out into the nebula and the total injection energy
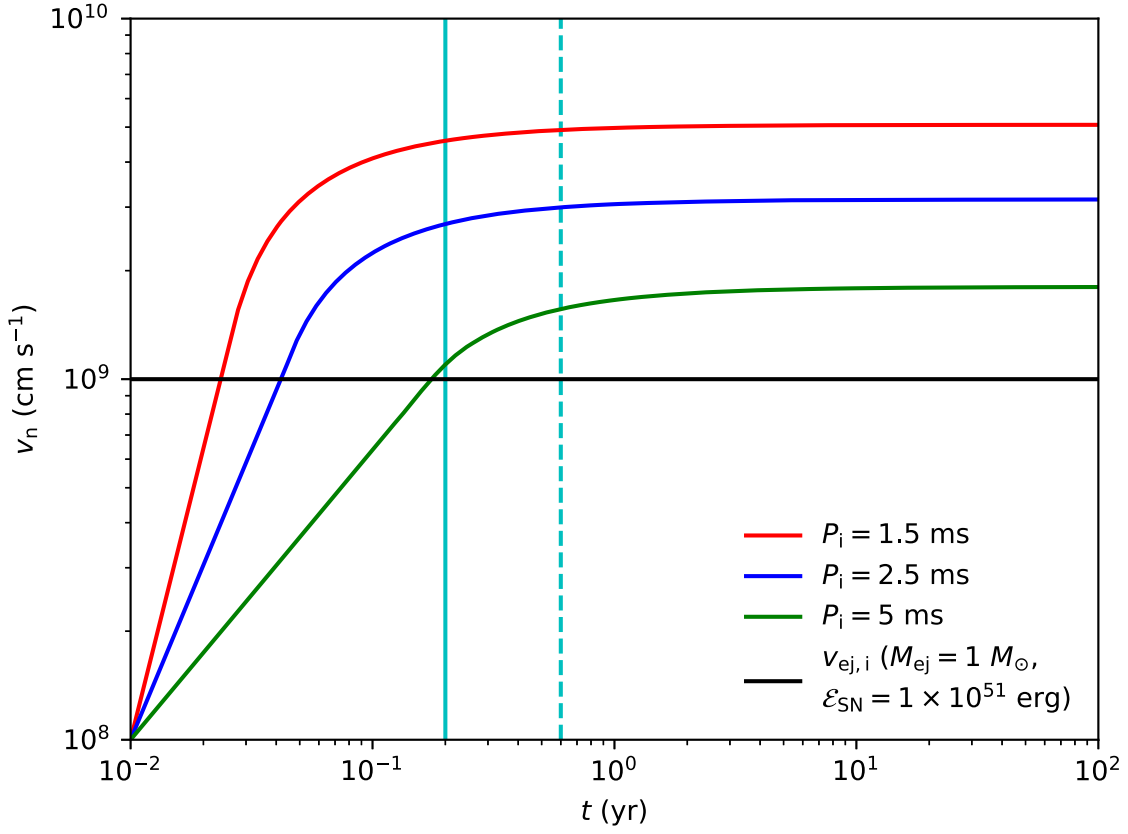
Figure 1. The nebula velocity derived from Equations (7) and (8) for $B_{int} \sim 10^{16}$ G, $M_{ej} = 1 \, M_\odot$, and $\mathcal{E}_{SN} = 1 \times 10^{51}$ erg. The red, blue, and green solid lines represent the cases of $P_i = 1.5$ ms, $P_i = 2.5$ ms, and $P_i = 5$ ms, respectively. The initial ejecta velocity is shown with black lines. The onset of the magnetic-energy injection $t_0 = 0.2$ yr and 0.6 yr is shown in cyan solid and dashed lines, respectively. We can see that ejecta are accelerated significantly in a relatively short time ($\sim 10^{-2}$–10^{-1} yr) before the magnetic flux begins to leak out. The peak ejecta velocity reaches up to $\sim$20,000–60,000 km s^{-1}, which is consistent with the observations of SN Ib/Ic.

$\mathcal{E}_{tot} = \mathcal{E}_{rot} + \mathcal{E}_{mag} = \int_0^t (L_{sd}(t) + L_m(t)) dt$. The solution of Equations (7) and (8) for the example case $B_{int} \sim 10^{16}$ G, $M_{ej} = 1 \, M_\odot$, and $\mathcal{E}_{SN} = 1 \times 10^{51}$ erg is shown in Figure 1. The red, blue, and green solid lines represent the cases of $P_i = 1.5$ ms, $P_i = 2.5$ ms, and $P_i = 5$ ms, respectively. The initial ejecta velocity is shown as black lines. The onset of the magnetic-energy injection $t_0 = 0.2$ yr and 0.6 yr from the benchmark model of Margalit & Metzger (2018) is shown in cyan solid and dashed lines, respectively. We can see that ejecta are accelerated significantly in a short time ($\sim 10^{-2}$–10^{-1} yr) before the magnetic flux begins to leak out. The peak ejecta velocity reaches up to $\sim$20,000–60,000 km s^{-1}, which is consistent with the observations of SN Ib/Ic (Kawabata et al. 2002; Rho et al. 2021).

The evolution of nebular magnetic fields is $B_n = \sqrt{(6\mathcal{E}_B/R_n^3)}$, where $\mathcal{E}_B$ is the magnetic energy in the nebula and R_n is the nebula radius. The magnetic energy in the nebula is given by Murase et al. (2021)

$$\frac{d\mathcal{E}_B}{dt} = \epsilon_B L(t) - c_B \frac{\dot{R}_n}{R_n} \mathcal{E}_B, \qquad (9)$$

where ϵ_B is the magnetic-energy fraction. In this work, we do not consider the magnetic-energy loss caused by adiabatic expansion, which has been used in Galactic PWNe (Tanaka & Takahara 2010, 2013) and high-energy emission of pulsar-

powered PWNe (Murase et al. 2015, 2016). The limit $c_B \to 0$ is a good approximation for a young source engine.

2.3. The Evolution of Particle Distribution

The evolution of the electron number density distribution $n_{e,\gamma}$ is given by the continuity equation in energy space,

$$\frac{\partial}{\partial t} n_{e,\gamma} + \frac{\partial}{\partial \gamma} (\dot{\gamma} n_{e,\gamma}) = \dot{Q}_{e,\gamma}, \qquad (10)$$

where $\dot{Q}_{e,\gamma}$ is the injection electron number density. The electron cooling process $\dot{\gamma}$ includes synchrotron radiation, synchrotron self-Compton (SSC), and adiabatic expansion

$$\dot{\gamma}(\gamma, t) = \dot{\gamma}_{syn}(\gamma, t) + \dot{\gamma}_{SSC}(\gamma, t) + \dot{\gamma}_{ad}(\gamma, t). \qquad (11)$$

The energy loss of synchrotron radiation is given by Rybicki & Lightman (1979)

$$\dot{\gamma}_{syn}(\gamma, t) = -\frac{4}{3} \frac{\sigma_T \gamma^2}{m_e c} U_B(t), \qquad (12)$$

where $U_B = B_n^2/8\pi$ is the energy density of the magnetic field. The energy loss caused by SSC is (Blumenthal & Gould 1970)

$$\dot{\gamma}_{\rm SSC}(\gamma, t) = -\frac{3}{4}\frac{\sigma_{\rm T} h}{m_e c}\frac{1}{\gamma^2}\int_0^\infty \nu_{\rm fin} d\nu_{\rm fin}$$
$$\times \int_0^\infty \frac{n_{\rm syn}(\nu_{\rm ini}, t)}{\nu_{\rm ini}} f(q, \Gamma_\epsilon)$$
$$\times \theta(1-q)\theta(q - 1/4\gamma^2)d\nu_{\rm ini}, \quad (13)$$

where $\nu_{\rm ini}$ and $\nu_{\rm fin}$ are the frequencies of the initial synchrotron radiation photons and that of scattered photons, $\Gamma_\epsilon = 4\gamma h\nu_{\rm ini}/(m_e c^2)$, $q = h\nu_{\rm fin}/(\Gamma_\epsilon(\gamma m_e c^2 - h\nu_{\rm fin}))$, $f(q, \Gamma_\epsilon) = 2q \ln q + (1 + 2q)(1-q) + 0.5(1-q)$ $(\Gamma_\epsilon q)^2/(1 + \Gamma_\epsilon q)$, and $\theta(x)$ is the step function. The seed synchrotron photon number density $n_{\rm syn}$ is

$$n_{\rm syn}(\nu, t) = \frac{L_{\nu,\rm syn}(t)}{4\pi R_n^2(t) c}\frac{1}{h\nu}\bar{U}, \quad (14)$$

where $L_{\nu,\rm syn}$ is the synchrotron radiation luminosity (see Section 2.4), and $\bar{U} \sim 2.24$ (Atoyan & Aharonian 1996) is used in our calculations. The adiabatic cooling is given by

$$\dot{\gamma}_{\rm ad}(\gamma, t) = -\frac{1}{3}\gamma\frac{d\ln V_n}{dt} = -\frac{\dot{R}_n}{R_n}\gamma. \quad (15)$$

2.4. The Synchrotron Radiation of MWN

The spectral power of synchrotron radiation is

$$P_\nu = \frac{2e^3 B_n}{\sqrt{3}\, m_e c^2}F\left(\frac{\nu}{\nu_c}\right), \quad (16)$$

where $\nu_c = \gamma^2 eB/2\pi m_e c$ is the characteristic frequency, $F(x) = x\int_x^{+\infty}K_{5/3}(k)dk$ and $K_{5/3}(k)$ is the 5/3 order modified Bessel function. The emissivity and absorption coefficients of synchrotron radiation is

$$j_\nu = \int \frac{n_{e,\gamma}P_\nu(\gamma)}{4\pi}d\gamma, \quad (17)$$

$$\alpha_\nu = -\int \frac{\gamma^2 P_\nu(\gamma)}{8\pi m_e \nu^2}\frac{\partial}{\partial\gamma}\left(\frac{n_{e,\gamma}}{\gamma^2}\right)d\gamma. \quad (18)$$

The synchrotron radiation luminosity considering the synchrotron self-absorption (SSA) is

$$L_\nu = 4\pi^2 R_n^2 \frac{j_\nu}{\alpha_\nu}(1 - e^{-\alpha_\nu R_n}). \quad (19)$$

In addition to SSA, free–free absorption due to the ejecta is also important for radio signals from a young magnetar. From the study of DM and RM evolution of FRB 121102 (Zhao et al. 2021), the associated magnetar is in a clean environment, which means that the magnetar is born in the merger of two compact stars. For the merger channel, the ejecta mass is $\sim$0.001–0.1 $M_\odot$, whose free–free absorption process is not obvious. However, for the SNe channel, free–free absorption due to the ejecta cannot be neglected. The free–free optical depth of the ejecta is (Wang et al. 2020; Zhao et al. 2021)

$$\tau_{\rm ff,ej} = \alpha_{\nu,\rm ff}\Delta R \simeq 2.06\eta^2 Y_{e,0.2}^2 M_{\rm ej,1}^2 T_{\rm ej,4}^{-3/2}\nu_9^{-2}v_{\rm ej,9}^{-5}t_{\rm yr}^{-5}, \quad (20)$$

where η is the ionization fraction, $Y_{e,0.2} = Y_e/0.2$ is the the electron fraction, $M_{\rm ej,1} = M_{\rm ej}/1M_\odot$ is the ejecta mass, and $T_{\rm ej,4} = T_{\rm ej}/10^4$K is the ejecta temperature. Due to the free–free absorption of electrons, the SNR will be optically thick for 3 yr and 1.5 yr for $M_{\rm ej} = 10\, M_\odot$ and $M_{\rm ej} = 2\, M_\odot$, which is shown in gray and black shaded regions in Figures 2 and 3, respectively.

3. Numerical Results

From the dynamics equations of MWN, we know that the nebula/ejecta velocity is mainly accelerated by the rotational-energy injection and is almost constant for the time of our interest. The assumption of $v_n \simeq v_{\rm ej,f}$ is a good approximation (Metzger et al. 2014; Kashiyama et al. 2016) for $R_n > R_{\rm ej}$. In our calculations, we take $v_{\rm ej,f} = 0.1c$, which is the mean ejecta velocity of SN Ib/Ic (Soderberg et al. 2012) and compact binary mergers. Following Margalit & Metzger (2018), $t_0 = 0.2$ yr and $\alpha = 1.3$ are used in this work. The energy fraction $\epsilon_B = 0.1$ and $\epsilon_B + \epsilon_e \sim 1$ is used. The injection spectrum indices $p_1 = 1.3$ and $p_2 = 2.5$ are taken from Law et al. (2019) and Mondal et al. (2020). The exact values of $\gamma_{\rm min}$ and $\gamma_{\rm max}$ are not important as long as they are small or large enough. The main parameters are the interior magnetic field $B_{\rm int}$, the source age $t_{\rm age}$, and the break Lorentz factor γ_b.
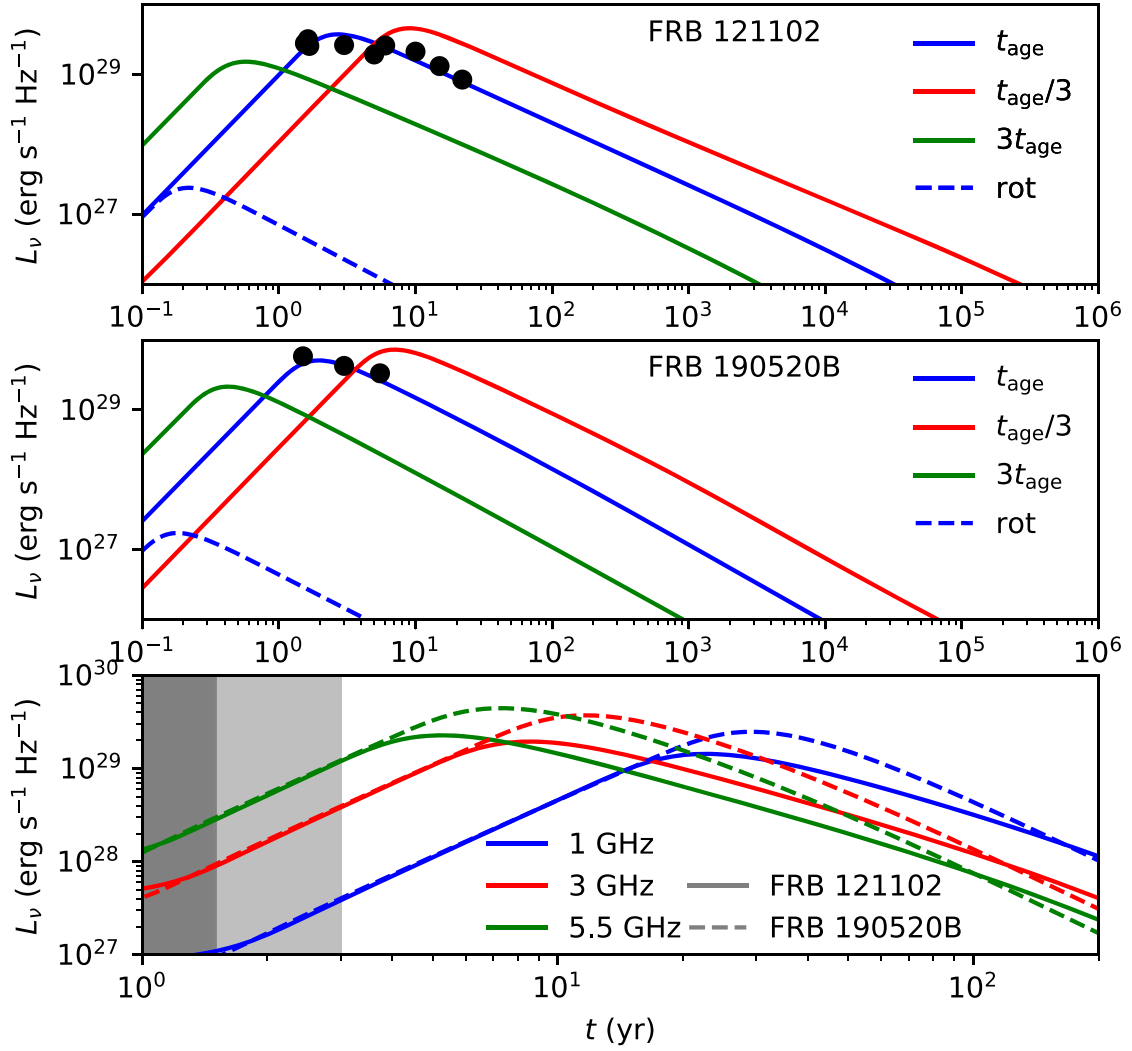
The spectral energy distribution is shown in Figure 2. The electron density n_e and the nebula magnetic field B_n are from the solutions of Equations (10) and (9). We find that parameters $B_{\rm int} = 2.76 \times 10^{16}$ G, $t_{\rm age} = 14$ yr and $\gamma_b = 5 \times 10^4$ can reproduce the spectrum of the PRS associated with FRB 121102 (Chatterjee et al. 2017), and $B_{\rm int} = 3.41 \times 10^{16}$ G, $t_{\rm age} = 22$ yr and $\gamma_b = 5 \times 10^3$ for that of FRB 190520B (Niu et al. 2021). The source age of FRB 121102 we guessed as roughly consistent with that of previous studies (Margalit & Metzger 2018; Yang & Dai 2019; Zhao et al. 2021). For FRB 190520B, the source age is given by the estimate from the DM evolution (see Section 4). The red, blue, and green solid lines represent the observed epocha at $t = t_{\rm age}/3$, $t = t_{\rm age}$, and $t = 3t_{\rm age}$. The case of rotational-energy injection is also plotted as a dashed line at $t = t_{\rm age}$ for comparison, whose dipole magnetic field is estimated under the assumption of $B_{\rm dip} = 0.1B_{\rm int}$ (Levin et al. 2020) and an initial spin period $P_i = 5$ ms is taken. The light curves at 1 GHz, 3 GHz, and 5.5 GHz (blue, red, and green lines, respectively) for FRB 121102 and FRB 190520B (solid and dashed lines, respectively) are shown in the bottom panel in Figure 2. The size of MWN we obtained is $\sim$0.4 pc for FRB 121102, which satisfies the constraints <0.7 pc given by very long baseline interferometry (VLBI, Marcote et al. 2017).

The DM and RM from the relativistic electrons in MWN are

$$\mathrm{DM}_{\rm MWN} = R_n \cdot \int \frac{n_{e,\gamma}}{\gamma^2}d\gamma, \quad (21)$$

$$\mathrm{RM}_{\rm MWN} = \frac{e^3}{2\pi m_e^2 c^4}R_n B_n \cdot \int \frac{n_{e,\gamma}}{\gamma^2}d\gamma, \quad (22)$$

where the electron density n_e and the nebula magnetic field B_n are from the solutions of Equations (10) and (9). We find that the DM from the MWN is <1–10 pc cm^{-3} and RM is <10^4–10^5 rad m^{-2}. The contributions from the MWN are negligible compared with the SNR (see Section 4).

Figure 2. The spectral energy distribution for the PRS associated with FRB 121102 (top panel) and FRB 190520B (middle panel). The main parameters are $B_{int} = 2.76 \times 10^{16}$ G, $t_{age} = 14$ yr and $\gamma_b = 5 \times 10^4$ for FRB 121102 , and $B_{int} = 3.41 \times 10^{16}$ G, $t_{age} = 22$ yr and $\gamma_b = 5 \times 10^3$ for FRB 190520B. The red, blue, and green solid lines represent the spectra-observed epoch at $t = t_{age}/3$, $t = t_{age}$, and $t = 3t_{age}$. The case of rotational-energy injection is also plotted with a dashed line at $t = t_{age}$ for comparison, whose dipole magnetic field is estimated as $B_{dip} = 0.1B_{int}$ and an initial spin period $P_i = 5$ ms is taken. The black circles are the observation values from Chatterjee et al. (2017) for FRB 121102 and Niu et al. (2021) for FRB 190520B. The light curves of PRS (bottom panel) at 1 GHz, 3 GHz, and 5.5 GHz (blue, red, and green lines, respectively) for FRB 121102 and FRB 190520B (solid and dashed lines, respectively). The SNR will be optically thick for 3 yr and 1.5 yr for $M_{ej} = 10 \, M_\odot$ and $M_{ej} = 2 \, M_\odot$, which is shown by the gray and black shaded regions.

4. Long-term DM Evolution

FRB 190520B has been reported in a dense environment, and the estimated $DM_{host} \simeq 902^{+88}_{-128}$ pc cm^{-3} (Niu et al. 2021) is nearly ten times higher than that of other FRB host galaxies. The DM of FRB 190520B systemically decreases with a rate of -0.09 ± 0.02 pc cm^{-3} day^{-1} together with some irregular variations (Niu et al. 2021). In our model, the long-term DM variation is from the expanding SNR (Yang & Zhang 2017; Piro & Gaensler 2018; Katz 2021a; Zhao et al. 2021) and the random variations may be caused by turbulent motions of filaments (Katz 2021b).

### 4.1. The DM from the Local Environment

For cosmological FRBs, the observed DM or RM contains the contributions of the Milky Way (MW), the Milky Way halo, the intergalactic medium (IGM), the host galaxy, and the local environment of FRBs:

$$DM_{obs} = DM_{MW} + DM_{halo} + DM_{IGM} + \frac{DM_{host} + DM_{source}}{1 + z}, \quad (23)$$

$$RM_{obs} = RM_{MW} + RM_{halo} + RM_{IGM} + \frac{RM_{host} + RM_{source}}{(1 + z)^2}. \quad (24)$$

Using the IllustrisTNG simulation, Zhang et al. (2020) found that the DM contributed by FRB 190520B-like host galaxies at $z \sim 0.2$ is ~ 50–250 pc cm^{-3}. Therefore, the DM from the source of FRB 190520B can be inferred to be ~ 524–940 pc cm^{-3}. Following our previous work (Zhao et al. 2021), the DM from the local environment of FRBs is
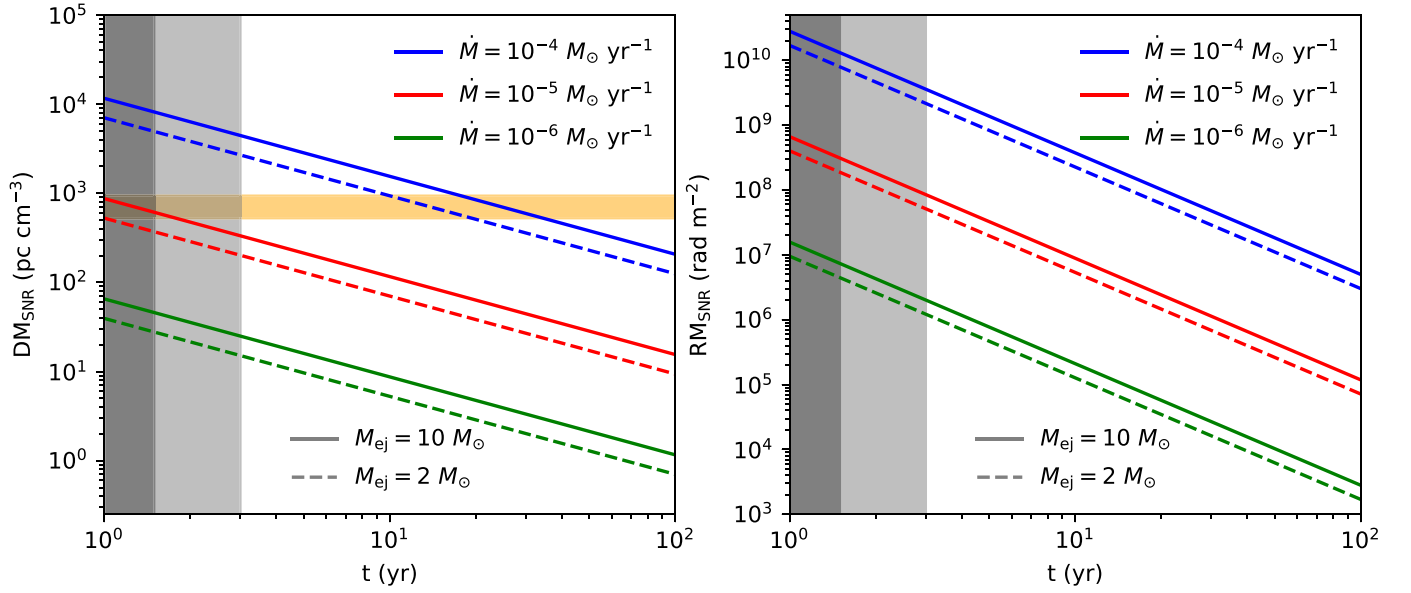
Figure 3. DM (left panel) and RM (right panel) contributed by SNR based on Equations (24) and (45)–(48) of Zhao et al. (2021). We adopt the typical parameters of SNRs: an explosion energy $E_{SN} \sim 1 \times 10^{51}$ erg, a power-law index of outer ejecta $n = 10$, ionization fractions of unshocked ejecta $\eta = 0.1$, a wind velocity of progenitors $v_w = 10$ km s^{-1}, and $\epsilon_B = 0.1$. The solid and dashed lines represent the cases of $M_{ej} = 10\,M_\odot$ and $M_{ej} = 2\,M_\odot$, respectively. The blue, red, and green lines represent different progenitors' mass-loss rates. The orange shading is the range of estimated DM$_{source}$. We can see that only the case of $\dot{M} = 10^{-4}\,M_\odot$ yr^{-1} and the source age $t_{age} = 10$–30 yr can provide a large enough DM as required by observations. The SNR will be optically thick for 3 yr and 1.5 yr for $M_{ej} = 10\,M_\odot$ and $M_{ej} = 2\,M_\odot$, which is shown in gray and black shaded regions.

given by

$$DM_{source} = DM_{MWN} + DM_{unsh,ej}$$
$$+ DM_{sh,ej} + DM_{sh,ISM} + DM_{unsh,ISM}, \quad (25)$$

where DM$_{MWN}$, DM$_{unsh,ej}$, DM$_{sh,ej}$, DM$_{sh,ISM}$ and DM$_{unsh,ISM}$ are the contributions from the MWN, unshocked ejecta, shocked ejecta, shocked ISM, and unshocked ISM, respectively. Usually, DM$_{unsh,ISM}$ is negligible because of the low ionization fraction. The unshocked region is not magnetized, so the RM from the source only contributed by three parts:

$$RM_{source} = RM_{MWN} + RM_{sh,ej} + RM_{sh,ISM}. \quad (26)$$

The contributions from the MWN are also negligible compared with the SNR. The total DMs and RMs from the SNR are shown in Figure 3. Our calculations are based on Equations (24) and (45)–(48) of Zhao et al. (2021). We adopt the typical parameters of SNRs: an explosion energy $\mathcal{E}_{SN} \sim 1 \times 10^{51}$ erg, a power-law index of outer ejecta $n = 10$, ionization fractions of unshocked ejecta $\eta = 0.1$, wind velocity of progenitors $v_w = 10$ km s^{-1}, and $\epsilon_B = 0.1$. The solid and dashed lines represent the cases of $M_{ej} = 10\,M_\odot$ and $M_{ej} = 2\,M_\odot$, respectively. The blue, red, and green lines represent different progenitors' mass-loss rates. The orange shading is the range of estimated DM$_{source}$. We can see that only the case of $\dot{M} = 10^{-4}\,M_\odot$ yr^{-1} and the source age $t_{age} = 10$–30 yr can provide a large enough DM. The constraint on the source age is consistent with that derived from PRS in the previous section.

4.2. Fitting Results

We assume that the variations of DM are only from DM$_{source}$. Thus, we can define the unchangeable DM$_{other}$ = DM$_{obs}$ − DM$_{source}$ to facilitate fitting. From the estimation of DM$_{source}$ above, we can get

DM$_{other} \sim 270$–686 pc cm^{-3}. The Markov Chain Monte Carlo (MCMC) method performed by Python package emcee[3] (Foreman-Mackey et al. 2013) is used to estimate the parameters DM$_{other}$ and the age of the source t_{age}. The χ^2 for the observed DMs is

$$\chi^2_{DM} = \sum_{i=1}^{n} \frac{(DM_{SNR,i} - DM_{obs,i})^2}{\sigma^2}, \quad (27)$$

where DM$_{SNR}$ is the DM from the SNR given by our model, and DM$_{obs}$ and σ are the observed DM and uncertainties in the frame of observers (Niu et al. 2021). The likelihood is

$$\mathcal{L} \propto \exp[-(\chi^2_{DM})/2]. \quad (28)$$

The posterior corner plots obtained from fitting the models of two typical ejecta mass models ($M_{ej} = 10\,M_\odot$ and $M_{ej} = 2\,M_\odot$) to the deta are shown in Figure 4. Our best-fit parameters are shown by blue solid lines and the parameters with 1σ ranges are shown with dashed lines. For $M_{ej} = 10\,M_\odot$, we find DM$_{other} = 464 \pm 15$ pc cm^{-3}　(DM$_{SNR} = 746 \pm 15$　pc cm^{-3}) and the source age is 21.9 ± 0.5 yr. For $M_{ej} = 2\,M_\odot$, we find DM$_{other} = 642 \pm 12$ pc cm^{-3}　(DM$_{SNR} = 568 \pm 12$　pc cm^{-3}) and the source age is 16.6 ± 0.4 yr. The DM evolution after the SN explosion is plotted in Figure 5. Due to the free–free absorption of electrons, the SNR will be optically thick for 3 yr and 1.5 yr for $M_{ej} = 10\,M_\odot$ and $M_{ej} = 2\,M_\odot$, respectively. The shaded regions indicate that the SNR is opaque to radio signals of $\nu \sim 1$ GHz. If we assume that the typical SN ejecta mass is $2M_\odot < M_{ej} < 10M_\odot$, the source age of FRB 190520B can be estimated as 16–22 yr. In the same way, we have DM$_{other} = 449$–654 pc cm^{-3} (DM$_{SNR} = 556$–761　pc cm^{-3}).

When DM$_{source}$ is taken into consideration, the DM$_{host}$ of FRB 190520B is not special, which is consistent with that derived from the IllustrisTNG simulation (Zhang et al. 2020).

─────────
3　http://emcee.readthedocs.io
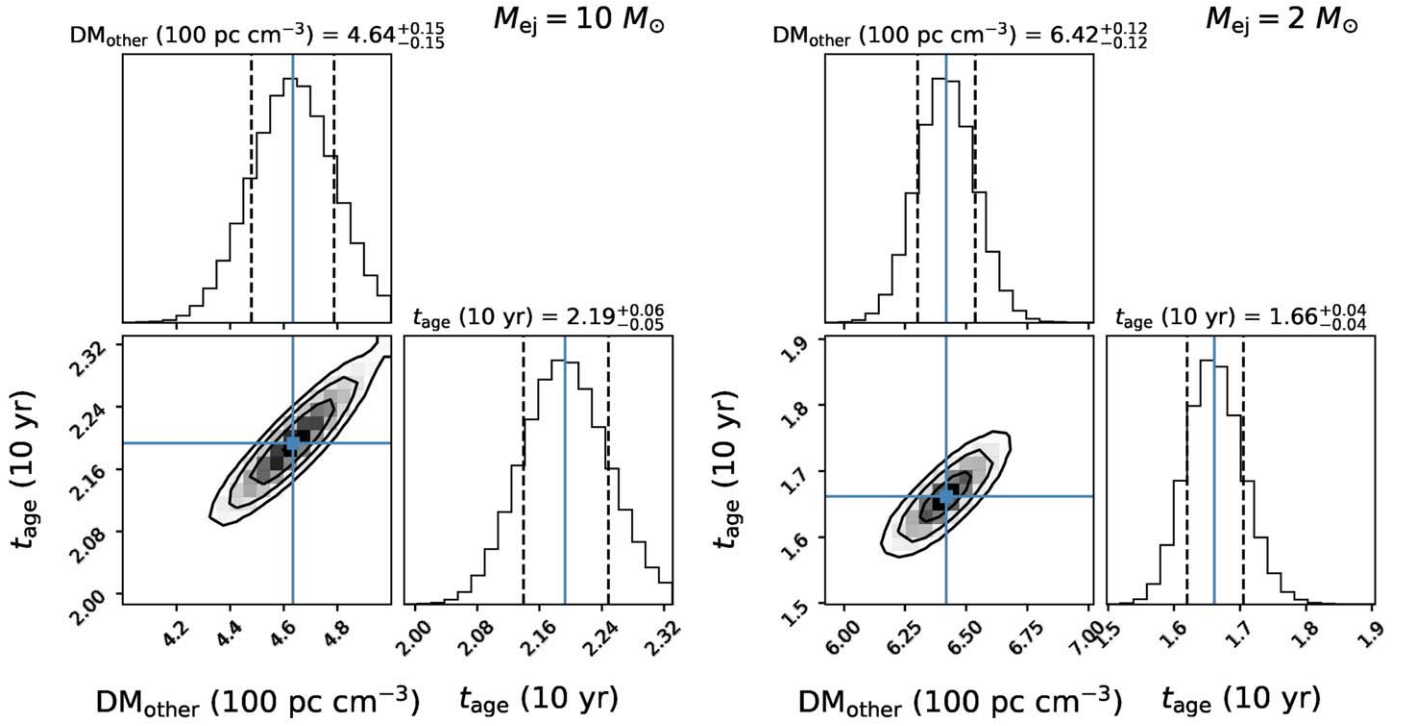
Figure 4. Posteriors parameters of the DM model fit to FRB 190520B for the case of $M_{ej} = 10\ M_\odot$ (left panel) and $M_{ej} = 2\ M_\odot$ (right panel) performed by MCMC method. The posterior probability of the parameters of $DM_{other} = DM_{obs} - DM_{source}$ and t_{age} is plotted in the histograms, and the 1σ range is shown by the dashed vertical lines. The medians are shown by blue lines. The contours indicate the parameter space with 1σ, 2σ, and 3σ range. If we assume that the typical SN ejecta mass is $2M_\odot < M_{ej} < 10M_\odot$, the source age of FRB 190520B can be estimated as 16–22 yr. In the same way, we have $DM_{other} = 449$–654 pc cm^{-3} ($DM_{SNR} = 556$–761 pc cm^{-3}).
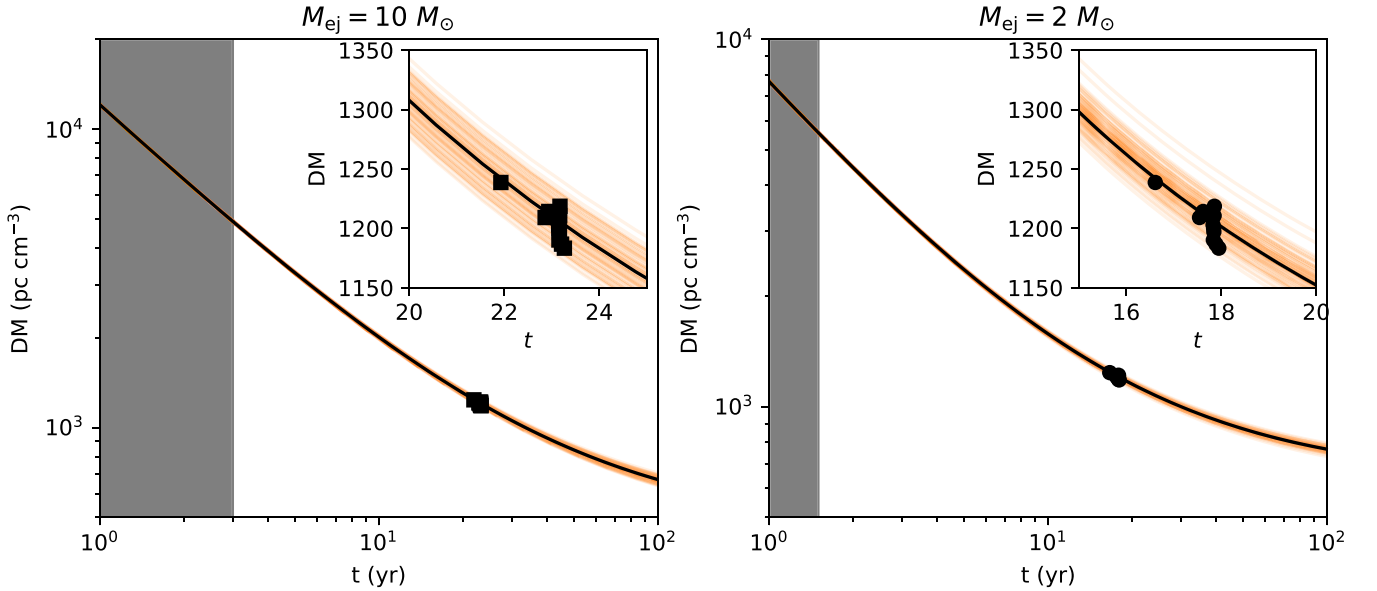
Figure 5. Samples of DM_{SNR} for $M_{ej} = 10\ M_\odot$ (left panel) and $M_{ej} = 2\ M_\odot$ (right panel) from the MCMC method (orange curves). Black squares and circles are the DM_{obs} of FRB 190520B from Niu et al. (2021). Black lines represent the best-fit values given by the MCMC method. The shaded regions indicate the SNR is opaque to radio signals of $\nu \sim 1$ GHz.

The DM decline will continue for another few decades, and then DM will trend to be stable when $DM_{other} \gg DM_{SNR}$. Finally, we have $DM \sim DM_{other}$ for $t \sim 100$–1000 yr. An unchangeable DM has been reported for FRBs (e.g., FRB 180916, see CHIME/FRB Collaboration et al. 2020b; Pastor-Marazuela et al. 2021; Nimmo et al. 2021). For FRB 121102, the estimated $RM_{MWN} \sim 10^4$–10^5 rad m^{-2} at $t_{age} = 14$ yr is consistent with the study of DM and RM evolution (Zhao et al.

2021, their estimated age starts on 2012). For FRB 190520B, the large RM is from the young SNR (RM $\sim 10^7$–10^8 rad m^{-2}).

5. Summary

In this Letter, we argue that the magnetar associated with FRB 190520B is embedded in the "composite" of MWN and SNR. Due to the energy injection of the young magnetar

(16–22 yr), the wind nebula and the SN ejecta will evolve together. The observed PRS is from the synchrotron radiation of the nebula. The dense SNR ejecta and the shocked shell contribute the observed DM and RM. Our model can simultaneously explain the luminous PRS, decreasing DM, and extreme RM of FRB 190520B. Our conclusions are summarized as follows:

1. The compact PRSs associated with FRBs are from the synchrotron radiation of the MWNe. From the observed luminosities and spectra, we find the interior magnetic field $B_{\rm int} = 2.76 \times 10^{16}$ G, the source age $t_{\rm age} = 14$ yr for FRB 121102, and $B_{\rm int} = 3.41 \times 10^{16}$ G, $t_{\rm age} = 22$ yr for FRB 190520B.

2. FRB 190520B is embedded in a dense SNR whose DM contribution is $\sim 746 \pm 15$ pc cm^{-3} and $\sim 568 \pm 12$ pc cm^{-3} for $M_{\rm ej} = 10\ M_\odot$ and $M_{\rm ej} = 2\ M_\odot$, respectively. Considering the DM from the SNR, the DM from the interstellar medium of FRB 190520B's host galaxy is not special any more, which is consistent with that derived from the state-of-the-art IllustrisTNG simulation (Zhang et al. 2020). The DM decay rate -0.09 ± 0.02 pc cm^{-3} d^{-1} can be well understood in the context of an SNR with an age of 16–22 yr, well in the range required by the PRS. The decline will continue for another few decades, and then DM will trend toward stable.

3. For FRB 190520B, the large RM is from the young SNR (RM $\sim 10^7$–10^8 rad m^{-2}). The RM attributed to MWN is $< 10^4$–10^5 rad m^{-2} in our model, which is much lower than the lower limit given by Niu et al. (2021) and the contributions from SNR.

ORCID iDs

Z. Y. Zhao ⓘ https://orcid.org/0000-0002-2171-9861
F. Y. Wang ⓘ https://orcid.org/0000-0003-4157-7714

References

Atoyan, A. M., & Aharonian, F. A. 1996, MNRAS, 278, 525
Blumenthal, G. R., & Gould, R. J. 1970, RvMP, 42, 237
Bochenek, C. D., Ravi, V., Belov, K. V., et al. 2020, Natur, 587, 59
Chatterjee, S., Law, C. J., Wharton, R. S., et al. 2017, Natur, 541, 58
Chevalier, R. A., & Soker, N. 1989, ApJ, 341, 867
CHIME/FRB Collaboration, Andersen, B. C., Bandura, K. M., et al. 2020a, Natur, 587, 54
CHIME/FRB Collaboration, Amiri, M., Andersen, B. C., et al. 2020b, Natur, 582, 351
Cordes, J. M., & Chatterjee, S. 2019, ARA&A, 57, 417
Dai, Z. G., & Lu, T. 1998, A&A, 333, L87
Dai, Z. G., Wang, J. S., & Yu, Y. W. 2017, ApJL, 838, L7
Eftekhari, T., Berger, E., Margalit, B., et al. 2019, ApJL, 876, L10
Foreman-Mackey, D., Hogg, D. W., Lang, D., & Goodman, J. 2013, PASP, 125, 306
Hessels, J. W. T., Spitler, L. G., Seymour, A. D., et al. 2019, ApJL, 876, L23
Hilmarsson, G. H., Michilli, D., Spitler, L. G., et al. 2021, ApJL, 908, L10
Josephy, A., Chawla, P., Fonseca, E., et al. 2019, ApJL, 882, L18
Kasen, D., & Bildsten, L. 2010, ApJ, 717, 245
Kashiyama, & Murase 2017, ApJL, 839, L3
Kashiyama, K., Murase, K., Bartos, I., Kiuchi, K., & Margutti, R. 2016, ApJ, 818, 94
Katz, J. I. 1982, ApJ, 260, 371
Katz, J. I. 2018, PrPNP, 103, 1
Katz, J. I. 2021a, arXiv:2110.10847
Katz, J. I. 2021b, MNRAS, 501, L76
Kawabata, K. S., Jeffery, D. J., Iye, M., et al. 2002, ApJL, 580, L39
Law, C. J., Connor, L., & Aggarwal, K. 2021, arXiv:2110.15323
Law, C. J., Omand, C. M. B., Kashiyama, K., et al. 2019, ApJ, 886, 24
Levin, Y., Beloborodov, A. M., & Bransgrove, A. 2020, ApJL, 895, L30
Li, D., Wang, P., Zhu, W. W., et al. 2021, Natur, 598, 267
Li, Q.-C., Yang, Y.-P., & Dai, Z.-G. 2020, ApJ, 896, 71
Lorimer, D. R., Bailes, M., McLaughlin, M. A., Narkevic, D. J., & Crawford, F. 2007, Sci, 318, 777
Marcote, B., Paragi, Z., Hessels, J. W. T., et al. 2017, ApJL, 834, L8
Margalit, B., & Metzger, B. D. 2018, ApJL, 868, L4
Metzger, B. D., Vurm, I., Hascoët, R., & Beloborodov, A. M. 2014, MNRAS, 437, 703
Michilli, D., Seymour, A., Hessels, J. W. T., et al. 2018, Natur, 553, 182
Mondal, S., Bera, A., Chandra, P., & Das, B. 2020, MNRAS, 498, 3863
Murase, K., Kashiyama, K., Kiuchi, K., & Bartos, I. 2015, ApJ, 805, 82
Murase, K., Kashiyama, K., & Mészáros, P. 2016, MNRAS, 461, 1498
Murase, K., Omand, C. M. B., Coppejans, D. L., et al. 2021, MNRAS, 508, 44
Nimmo, K., Hessels, J. W. T., Keimpema, A., et al. 2021, NatAs, 5, 594
Niu, C. H., Aggarwal, K., Li, D., et al. 2021, arXiv:2110.07418
Oostrum, L. C., Maan, Y., van Leeuwen, J., et al. 2020, A&A, 635, A61
Pastor-Marazuela, I., Connor, L., van Leeuwen, J., et al. 2021, Natur, 596, 505
Petroff, E., Hessels, J. W. T., & Lorimer, D. R. 2021, arXiv:2107.10113
Piro, A. L., & Gaensler, B. M. 2018, ApJ, 861, 150
Platts, E., Weltman, A., Walters, A., et al. 2019, PhR, 821, 1
Rho, J., Evans, A., Geballe, T. R., et al. 2021, ApJ, 908, 232
Rybicki, G. B., & Lightman, A. P. 1979, Radiative Processes in Astrophysics (New York: Wiley)
Soderberg, A. M., Margutti, R., Zauderer, B. A., et al. 2012, ApJ, 752, 78
Tanaka, S. J., & Takahara, F. 2010, ApJ, 715, 1248
Tanaka, S. J., & Takahara, F. 2013, MNRAS, 429, 2945
Wang, F. Y., Wang, Y. Y., Yang, Y.-P., et al. 2020, ApJ, 891, 72
Wang, J.-S., & Lai, D. 2020, ApJ, 892, 135
Xiao, D., Wang, F., & Dai, Z. 2021, SCPMA, 64, 249501
Yang, Y.-H., & Dai, Z.-G. 2019, ApJ, 885, 149
Yang, Y.-P., & Zhang, B. 2017, ApJ, 847, 22
Zhang, B. 2020, Natur, 587, 45
Zhang, B., & Mészáros, P. 2001, ApJL, 552, L35
Zhang, G. Q., Yu, H., He, J. H., & Wang, F. Y. 2020, ApJ, 900, 170
Zhao, Z. Y., Zhang, G. Q., Wang, Y. Y., Tu, Z.-L., & Wang, F. Y. 2021, ApJ, 907, 111